IEEE Access
Multidisciplinary | Rapid Review | Open Access Journal

Received 13 August 2022, accepted 13 October 2022, date of publication 26 October 2022, date of current version 3 November 2022.

Digital Object Identifier 10.1109/ACCESS.2022.3217205

RESEARCH ARTICLE

A 2-D Inductive Power Transfer Network for Powering Massive Neighboring IoT Devices

YIMING GAO[1,2,3], MINFAN FU[1,4], (Senior Member, IEEE), HAOYU WANG[1,4], (Senior Member, IEEE), AND JUNRUI LIANG[1,4], (Senior Member, IEEE)

[1]School of Information Science and Technology, ShanghaiTech University, Shanghai 201210, China
[2]Shanghai Advanced Research Institute, Chinese Academy of Sciences, Shanghai 201210, China
[3]University of Chinese Academy of Sciences, Beijing 100049, China
[4]Shanghai Engineering Research Center of Energy Efficient and Custom AI IC, Shanghai 201210, China

Corresponding author: Junrui Liang (liangjr@shanghaitech.edu.cn)

This work was supported in part by the National Natural Science Foundation of China under Grant 62271319 and Grant U21B2002, and in part by the Natural Science Foundation of Shanghai under Grant 21ZR1442300.

ABSTRACT Due to the wide distribution of Internet of Things (IoT) devices, reliable and convenient power solutions for these devices have been a continuous pursuit recently. In this paper, a two-dimensional (2-D) inductive power transfer (IPT) design based on multiple coupled resonators is proposed for powering IoT devices in a reconfigurable neighboring scenario. There are two types of cells in this system: constant voltage (CV) and constant current (CC) cells. These two types of cells are alternately arranged. In this IPT system, the coupling electromagnetic field is mostly constrained in a small region, so that the radiation leakage to the free space can be relieved without introducing extra complex control. The wireless power makes the whole system convenient and reconfigurable according to the user's requirements. The circuit model is mathematically formulated. A nine-cell prototype is implemented and tested. Experimental results approve the CC or CV properties in each cell. The power conversion efficiency of the whole system reaches 75%.

INDEX TERMS Constant voltage output, constant current output, inductive power transfer, multiple loads, power relay.

I. INTRODUCTION

Wireless power transfer (WPT) has been widely used in the areas of electric vehicles [1], high-speed train [2], and drone [3], etc. In addition to the trend towards higher power conversion capability and efficiency, WPT is also moving towards multiple loads [4], [5], [6], [7], [8], [9], [10], [11], [12], [13], [14], [15], [16], [17], omnidirectional [18], [19], [20] and long-distance [21], [22] applications.

Over the last decade, there has been a dramatic increase in the number of Internet of Things (IoT) devices. In the future, many of them will be installed inside the floor or wall in the house to acquire sensory information from humans, for example, fall detection [23], [24] and activity recognition [25], [26]. Besides, the next-generation artificial intelligence of things integrates information collection, analysis, and response to external stimulation. Given the rapid growth of IoT devices, these power-hungry IoT devices' installation and maintenance costs are incredibly high. In particular, we need long electrical cables for wired devices or frequent replacement or recharging for battery-powered wireless devices to continuously power these devices with state-of-the-art power technology. Innovative power solutions are expected and necessary for helping out with this dilemma. WPT technology provides a flexible and convenient connection to well-packed, water-tight electronic equipment. It has an enormous potential to offer cordless and robust power supply to massive IoT devices in the coming future.

Different from the one-dimension (1-D) WPT proposed in literature [8], [9], [10], [11], [12], [13], [14], [15], [17], the massive neighboring charging is more common in

The associate editor coordinating the review of this manuscript and approving it for publication was Alessandro Pozzebon.

practical scenario according to the distribution characteristics of IoT devices. The WPT technology for powering the massive neighboring IoT devices is abstracted as a two-dimensional (2-D) WPT network since the power is transferred along both x and y dimensions in a 2-D plane. A 2-D relay resonator array was presented in [28], [29], [30], and [31], aiming to power all devices arranged in a tiled pattern in an indoor environment. i.e., the coils are placed in one plane. However, the tiled pattern has inherent limitations, e.g., the cross-coupling effect and electromagnetic radiation leakage. In particular, the radiation issue in WPT has drawn much public attention. In [31], an adaptive phased array WPT was proposed to control the leakage radiation. The electromagnetic (EM) field in WPT belongs to a non-ionizing radiative field; according to the International Commission on Non-Ionizing Radiation Protection (ICNIRP) Guidelines [32], the general public's whole-body average Specific Absorption Rate (SAR) should be less than 0.08 W/kg, which sets the ceiling value of the transmission power. The tiled pattern produces a high-frequency electromagnetic field around the pick-up devices and along the power-delivering paths. Therefore, the transmission power should be below the upper limit along the power-delivering paths to obey the guideline. In addition, cross-coupling rejection and foreign object detection require complex control strategies to stabilize the transmission power and efficiency. In [29] the adjacent resonators cannot be simultaneously activated. Dynamic power routing is also a prerequisite for bypassing foreign metal objects. All of the problems mentioned above increase the complexity of practical implementations.

Considering all these issues, this paper proposes a confronting-coil-based resonator array inductive power transfer (IPT) system to overcome the limitations of the previous designs toward a 2-D WPT network. Compared with the previous designs, the main contributions of this paper are summarized as follows.

1) Relieving the electromagnetic field leakage by using confronting coils design.
2) Reducing the control effort by minimizing the cross-coupling effect.
3) Alternate constant voltage (CV) and constant current (CC) cell.

A nine-cell prototype is manufactured and tested to validate the proposed 2-D IPT system design. The rest parts of this paper are organized as follows. Section II gives an overview of the whole system. Section III discusses the power and efficiency of the system. Section IV presents the prototype and experiment results. Finally, Section V concludes.

II. SYSTEM OVERVIEW

Fig. 1 illustrates the overview of the system structure. The massive neighboring structures are frequently seen on the floor, wall, table, and other reconfigurable planes. In future

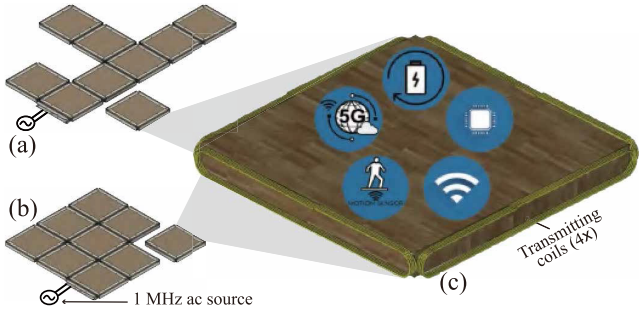

FIGURE 1. 2D IPT reconfigurable closely neighboring array. (a) One layout of the closely neighboring array. (b) Another layout of the closely neighboring array. (c) One WPT-powered smart cell.

IoT designs, various sensors, digital microprocessors, and network interfaces might be embedded in these essential building cells to equip them with intelligence. The power solution of these embedded and wide-distributed devices is an important issue. Compared with a wired power supply, WPT removes all metal contacts between cells such that the cells can be configured into different shapes.

In this proposed WPT system, the coupling coils are installed along the edges of each tile, i.e., the coil plane is perpendicular to the upper tile plane, instead of horizontally like those in the previous designs [18], [20], [29], [33]. Owing to this new design, only the coupling effect between two adjacent coils needs to be considered. Those cross-couplings across other coils are very small. Therefore, they can be neglected. Each rectangular cell has four side coils to enable power transmission among itself and its four adjacent cells.

A. BASIC BUILDING CELLS

As Fig. 2 shows, there are two types of cells. The CC and CV cells are installed in an alternate pattern. In each CC cell, the four side coils, compensating capacitors, and the load is connected in series. While in each CV cell, four series coil and compensating capacitor branches are connected in parallel to form four LC resonant tanks. The load in a CV cell is connected in parallel with those four resonant branches. The boundary branches, i.e., those without adjacent coils, in CC cells are shorted to reduce conduction loss, while the boundary branches in CV cells are opened to avoid short circuits at a resonant state.

All the coils are identical, having the same shape and the same turns. Ideally speaking, their inductance values, equivalent series resistance (ESR), and quality factor are the same, which are denoted as L, r, and Q, respectively in the following parts.

In the coupling model, only the mutual inductance of the pairing coils is taken into consideration. The mutual inductance and coupling coefficient between the adjacent coils are denoted as M and k, respectively. They satisfy the

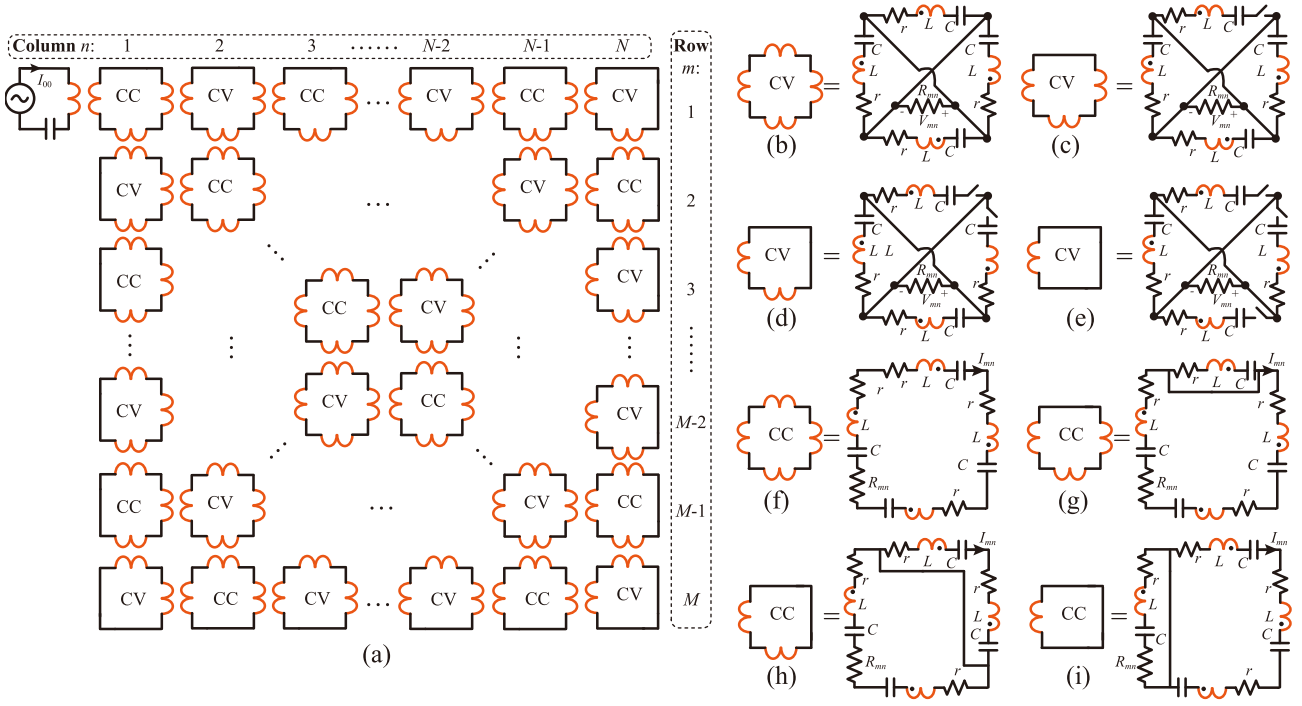

FIGURE 2. (a) Equivalent circuit topology. (b)–(i) Different cell implementations.

following relation

$$k = \frac{M}{L}. \tag{1}$$

B. SYSTEM DESCRIPTION

Traditional decoupling modeling methods include the reflected impedance method and the T model. From the system point of view, in the proposed massive neighboring topology, the reflected impedance method does not work since all cells are mutually coupled together. On the other hand, the network derived from the T model is too large to form a concise system equation. Therefore, we should refer to the basic Kirchhoff's Voltage Law (KVL) and Kirchhoff's Current Law (KCL) of an individual cell. Set the resonant frequencies of all resonant tanks to ω_0 the frequency of the power source, i.e.,

$$\omega_0 = \sqrt{\frac{1}{LC}} \tag{2}$$

such that all the compensation capacitors share the same value.

According to KVL, the voltage current relationship in a CC cell is given by (3)

$$\frac{jkQ}{r}\left[V_{(m-1)n} + V_{(m+1)n} + V_{m(n-1)} + V_{m(n+1)}\right] - \left(pk^2Q^2 + \frac{R_{mn}}{r} + p\right) I_{mn} = 0, \tag{3}$$

where $p = 1, 2, 3$, or 4, representing the number of cells nearby the #mn cell; I_{mn} and R_{mn} are the current and equivalent load resistance in #mn cell; $V_{(m-1)n}$, $V_{(m+1)n}$, $V_{m(n-1)}$, $V_{m(n+1)}$ are the load voltage of adjacent CV cells; Q is the quality factor of the coil, i.e.,

$$Q = \frac{\omega L}{r}. \tag{4}$$

The governing equation of a CV cell can be derived according to KCL, i.e.,

$$jkQ\left[I_{(m-1)n} + I_{(m+1)n} + I_{m(n-1)} + I_{m(n+1)}\right] - \left(q + \frac{r}{R_{mn}}\right) V_{mn} = 0, \tag{5}$$

where $q = 1, 2, 3$, or 4. It represents the number of cells near the cell #mn. V_{mn} is the voltage in the #mn cell. $I_{(m-1)n}$, $I_{(m+1)n}$, $I_{m(n-1)}$, $I_{m(n+1)}$ are the load current of the adjacent CC cells.

Only the combination of (3) and (5) is not adequate to solve the problem. The boundary conditions should be specified to determine the complete solution. In a practical scenario, the boundary conditions can be voltage sources or current sources. A voltage source should be used to drive a CC cell. In that case, one of voltage variables in (3) within $V_{(m-1)n}$, $V_{(m+1)n}$, $V_{m(n-1)}$, and $V_{m(n+1)}$ should be replaced by a voltage source. A current source should be used to drive a CV cell. A current variables in (5) within $I_{(m-1)n}$, $I_{(m+1)n}$, $I_{m(n-1)}$, and $I_{m(n+1)}$ is substituted by a current source.

When the cells and sources are well installed, all equations can be assembled into a matrix. The mathematical model of

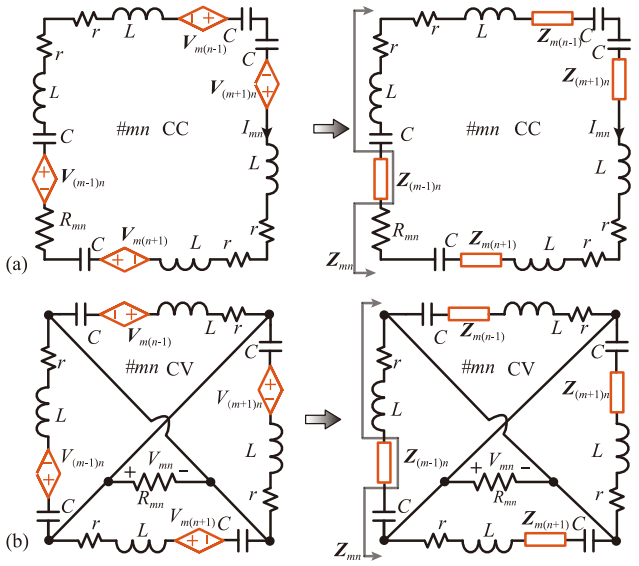

FIGURE 3. Reflected impedance model of an individual cell. (a) CC cell. (b) CV cell.

the whole system in Fig. 2 is given by (6), as shown at the bottom of the page.

C. CC AND CV PROPERTIES

A 3 × 3 array is taken as an example to demonstrate the CC and CV properties of different cells. By extracting the sub-matrix from (6), we can formulate the governing equation of the 3 × 3 array. Assuming the ESR is negligible compared to the ωM and R_{mn}, the solution of the 3×3 array can be derived as follows

$$I_{11} = I_{13} = I_{22} = I_{31} = I_{33} = \frac{V_{in}}{j\omega M} \tag{7}$$

$$V_{12} = V_{21} = V_{23} = V_{32} = V_{in} \tag{8}$$

These simplified results suggest that when the resonant conditions are satisfied, and ESR is small enough, the cells #11, #13, #22, #31, and #33 realize the load-independent CC property, while the cells #12, #21, #23, and #32 realize the load-independent CV property. Similar results hold even more cells are added, i.e.,

$$I_{mn} = \frac{V_{in}}{\omega M}, \quad \text{when } m+n = \text{even number} \tag{9}$$

$$V_{mn} = V_{in}, \quad \text{when } m+n = \text{odd number} \tag{10}$$

Eq. (9) and (10) indicate that the CC and CV properties are realized among the cells alternately.

D. ZERO PHASE ANGLE ANALYSIS

In a practical scenario, any cell added or removed from the massive neighboring IPT system should not affect the resonant state of the original system. Therefore, each cell should be purely resistive or have the zero phase angle (ZPA) condition, no matter looking from any side. Meanwhile, realizing the ZPA condition in each cell can minimize the power dissipation by the ESR.

The reflected impedance circuit models of individual CC and CV cells are shown in Fig. 3. In the CC cell, there are four induced voltage source from the adjacent cells named $V_{i(j-1)}$, $V_{(i-1)j}$, $V_{(i+1)j}$, and $V_{i(j+1)}$. According to the reflected impedance theory, the induced voltage sources can be regarded as reflected impedance from adjacent cells. Both the CC and CV cells are symmetrical, which means that it is exactly the same no matter looking from any side. The impedance Z_{mn}, therefore, looking from the left, is taken as an example to show the ZPA property

$$Z_{mn} = Z_{m(n+1)} + Z_{(m+1)n} + Z_{(m-1)n} + 4Z + R_{mn}, \tag{11}$$

where

$$Z = j\omega L + \frac{1}{j\omega C} + r. \tag{12}$$

In order to achieve ZPA, two conditions should be satisfied. Firstly, the impedance Z should be purely resistive. Secondly, the reflected impedance from the adjacent cells should be purely resistive.

Similarly, in the CV cell, the impedance of the CV cell looking from the left can be derived as follows

$$Z_{mn} = \Big\{ \big[Z_{(m+1)n} + Z\big]^{-1} + \big[Z_{m(n-1)} + Z\big]^{-1} + \big[Z_{m(n+1)} + Z\big]^{-1} + R_{mn}^{-1} \Big\}^{-1}. \tag{13}$$

The similar two conditions should be satisfied to ensure the ZPA property, i.e., both the Z and reflected impedance should be purely resistive.

From the system point of view, it suggests that the ZPA property from the adjacent cells leads to the ZPA property of the current cell and then reflects other adjacent cells. It shows the transitivity of the ZPA property. As long as it satisfies that Z in (12) is purely resistive, each cell can realize the ZPA property.

The ZPA condition is of importance for inverter design. The ZPA property of the inverter in a 3 × 3 massive neighboring IPT system can be studied by analyzing the input

$$\begin{bmatrix} I_{11} \\ V_{12} \\ I_{13} \\ \vdots \\ V_{21} \\ \vdots \end{bmatrix} = \begin{bmatrix} -(3k^2Q^2 + \frac{R_{11}}{r} + 3) & \frac{jkQ}{r} & \frac{jkQ}{r} & \cdots & \frac{jkQ}{r} & \cdots \\ jkQ & -(3 + \frac{r}{R_{12}}) & jkQ & \cdots & 0 & \cdots \\ 0 & \frac{jkQ}{r} & -(3k^2Q^2 + \frac{R_{13}}{r} + 3) & \cdots & 0 & \cdots \\ \vdots & \vdots & \vdots & \ddots & \vdots & \cdots \\ jkQ & 0 & 0 & \cdots & -(3 + \frac{r}{R_{21}}) & \cdots \\ \vdots & \vdots & \vdots & \vdots & \vdots & \ddots \end{bmatrix}^{-1} \begin{bmatrix} -\frac{jkQV_{in}}{r} \\ 0 \\ 0 \\ \vdots \\ 0 \\ \vdots \end{bmatrix}. \tag{6}$$

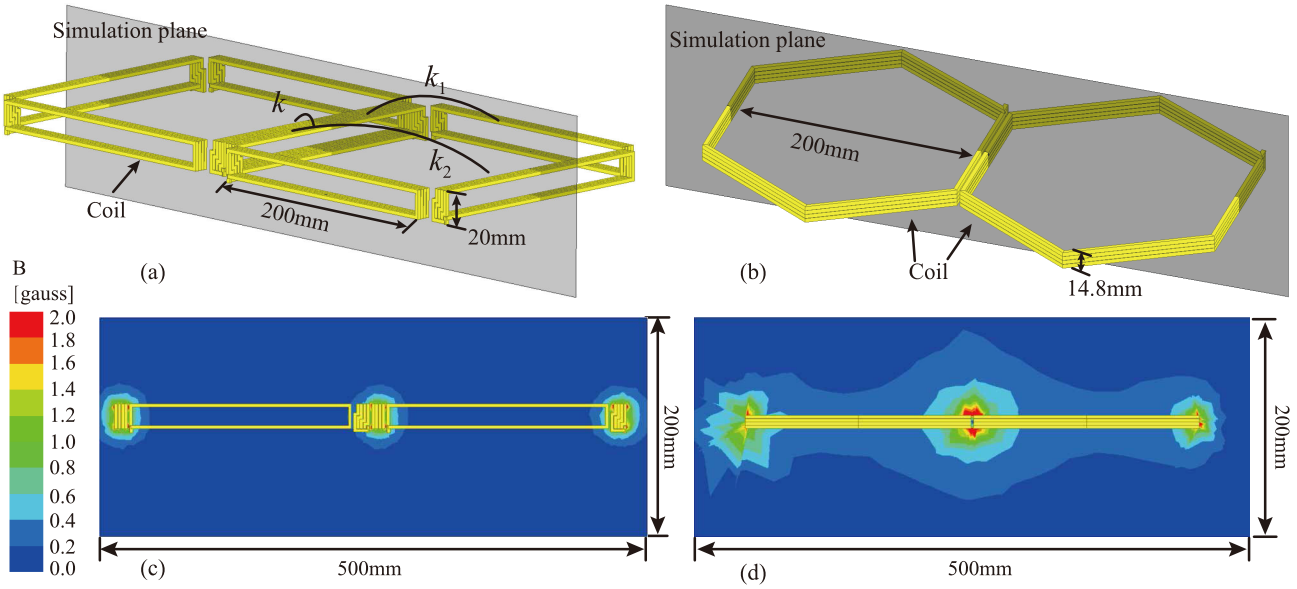

FIGURE 4. Magnetic field simulation results. (a) Confronting-coil-based resonator array in this paper. (b) Tiled pattern coil in [29]. (c) Magnetic field distribution of confronting-coil-based resonator array. (d) Magnetic field distribution of tiled pattern coil.

current I_{00}. Under the small ESR assumption, the results can be simplified as follows

$$I_{00} = V_{in}\left(\frac{R_{11}+R_{13}+R_{22}+R_{31}+R_{33}}{M^2\omega^2} + \frac{1}{R_{12}}+\frac{1}{R_{21}}+\frac{1}{R_{23}}+\frac{1}{R_{32}}\right) \tag{14}$$

Therefore, the input impedance is given as follows

$$Z_{in} = \frac{V_{in}}{I_{00}} = \left(\frac{R_{11}+R_{13}+R_{22}+R_{31}+R_{33}}{M^2\omega^2} + \frac{1}{R_{12}}+\frac{1}{R_{21}}+\frac{1}{R_{23}}+\frac{1}{R_{32}}\right)^{-1} \tag{15}$$

The pure resistive characteristic of the input impedance indicates that by looking at the inverter output, the proposed topology achieves the ZPA property.

E. COIL DESIGN

Considering the practical scenario, the physical dimension should be included in the design of coil structures. The coils are wound on the tile edge as shown in Fig. 1 (b). The dimension of each cell is 20 cm × 20 cm × 2 cm, thus the dimension of the coil is set to 20 cm × 2 cm.

The simulation of two different coils arrangement is evaluated under the 1 MHz frequency in Maxwell software to estimate the magnetic field level around the coils. The results are shown in Fig. 4. The tiled pattern is composed of two regular hexagons whose edge length is $50\sqrt{3}$ mm. The confronting-coil-based resonator array consists of two square shape tiles with dimensions 20 cm × 2 cm. Both coils have four turns. The distance between two adjacent coils is both set to 2 mm. The excitation current is both set to 1 A for comparative analysis.

TABLE 1. Parameters in two IPT networks.

	Para.	Value	Para.	Value
Confronting-coil-based array (this study)	L	2.42 μH	k	0.36
	k_1	0.012	k_2	2.1×10^{-4}
	r	27.4 mΩ	Q	554.9
Tiled pattern [29]	L	6.17 μH	k	0.12
	r	8.9 mΩ	Q	4355.9

The magnetic field of the tiled pattern and confronting-coil-based resonator array is illustrated in Fig. 4. In Fig. 4(c), little magnetic field leaks into the space since the field mainly concentrates in the center of the coil. Therefore, magnetic fields are confined to a small region, making it possible to transfer higher power under the same electromagnetic radiation. In Fig. 4(d), it can be observed that the range of the magnetic field in the tiled pattern distributed is much more extensive than the confronting-coil-based resonator array in the same magnetic scale. The leakage field might cause safety issues; therefore, the maximum transmission power should be at a safe level.

The parameters in two IPT networks are listed in Table 1. The results show that in the confronting-coil-based resonator array, the cross-coupling coefficient k_1 and k_2 are small enough to be neglected compared with the main coupling coefficient k. Thus, it is unnecessary to consider the cross-coupling effect in the proposed confronting-coil-based resonator array. In addition, the proposed confronting-coil-based resonator array has a more significant coupling coefficient than the tiled pattern. It enables a higher transferred power and conversion efficiency. However, compared with the tiled pattern, the quality factor is relatively lower.

III. POWER ANALYSIS

In section II, the CC and CV properties were derived based on the lossless system assumption. Nevertheless, the coils'

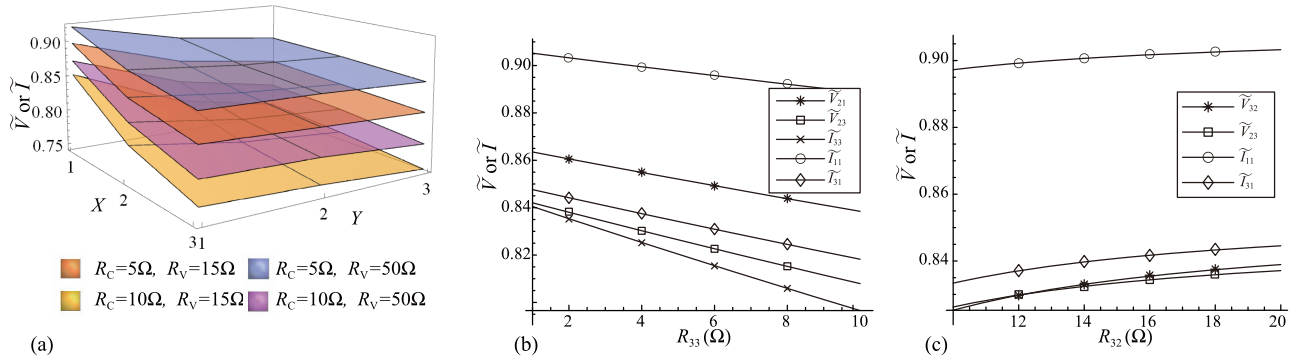

FIGURE 5. (a) Voltage/current deviation in 2-D plane. (b) Voltage/current deviation caused by R_{33}. (c)Voltage/current deviation caused by R_{32}.

ESR in real cases degenerates the system performance. In this 2-D IPT system, for easy analysis, the load of each CC cell is set to be an identical value R_C. For the CV cell, it is set to R_V i.e.,

$$\begin{aligned} R_{11} = R_{13} = \cdots = R_{mn} = R_C, \quad m+n = \text{even} \\ R_{12} = R_{21} = \cdots = R_{mn} = R_V, \quad m+n = \text{odd} \end{aligned} \tag{16}$$

A. LOAD VOLTAGE/CURRENT DEVIATION

Ideally, the output voltage of a CV cell and output current of a CC cell are constants, no matter how much the loads change and how many cells are connected. However, in a real scenario, ESR in every coil deviates from the output power. By solving (6), the load currents of CC cells and load voltages of CV cells can be obtained. To normalize the performance evaluation of CC and CV cells, the load current and voltage with practical ESR are divided by their corresponding ideal values, i.e.,

$$\tilde{V} = \frac{|V_{mn}|}{V_{in}}, \quad \tilde{I} = \frac{|I_{mn}|\omega M}{V_{in}} \tag{17}$$

Assuming that the system consists of nine cells (3 × 3). The quality factor of each coil is 120 and the coupling coefficient between two adjacent coils is 0.36. One voltage source powers the system through cell #11 as shown in Fig. 2(a).

The theoretical normalized output deviation of each cell at different loading conditions is shown in Fig. 5(a). It shows that the cells, which are further from the voltage source, have a more considerable performance decrease, compared with those near the voltage source. The load resistance variation also causes the performance deviation in the 2-D plane. The output current magnitude of a CC cell and output voltage of a CV cell is demonstrated under the condition that only one load resistance R_{33} or R_{32} varies, respectively, while the other loads keep unchanged. According to the first harmonic approximation, the dc load after a full bridge rectifier is equivalent to an ac load. At the initial state, we set the dc load to 15 Ω and 5 Ω for the CV and CC cells, respectively. Therefore, the equivalent ac loads R_C ad R_V are $\frac{40}{\pi^2}\Omega$ and $\frac{120}{\pi^2}\Omega$, respectively. Fig. 5(b) and (c) give the normalized voltage and current when either R_{33} or R_{32} varies. Only small deviations are induced in the load and adjacent cells when a load resistance changes.

B. EFFICIENCY

The output voltage/current has deviation, and the efficiency degenerates due to the ESR. By solving (6), the output current in the CC cell or output voltage in the CV cell with ESR can be obtained to calculate each cell's output power. The total transferred power is the sum of the output power of all cells, i.e.,

$$P_{mn} = \frac{I_{mn}^2 R_C}{2}, \quad i+j = \text{even} \tag{18}$$

$$P_{mn} = \frac{V_{mn}^2}{2R_V}, \quad i+j = \text{odd} \tag{19}$$

$$P_{out} = \sum_{i=1}^{N}\sum_{j=1}^{M} P_{mn}. \tag{20}$$

The input current or voltage can be derived according to their adjacent cells' current or voltage. For example, the input current I_{00} in Fig. 2 can be derived as follows

$$I_{00} = \frac{V_{in} - j\omega M I_{11}}{r} \tag{21}$$

Therefore the total input power is derived as follows

$$P_{in} = \frac{I_{00} V_{in}}{2} \tag{22}$$

Based on the input power and output power, the system efficiency is written as follows

$$\eta = \frac{P_{out}}{P_{in}}. \tag{23}$$

The efficiency variation under different R_C and R_V is shown in Fig. 6. From the figure, R_C has a more significant impact on efficiency. The reason is that R_C in the CC cell has the same role as the ESR because they are both connected in series in the CC cell. Therefore, R_C should be set in a suitable range in order to maintain the system performance in a relatively good condition. A maximum efficiency area is marked in Fig. 6. Within this area, the theoretically overall efficiency is above 80%

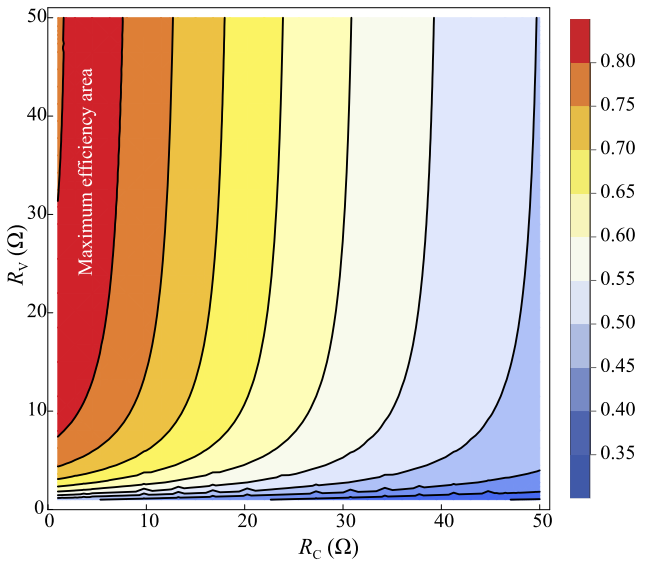

FIGURE 6. Overall conversion efficiency under different R_C and R_V.

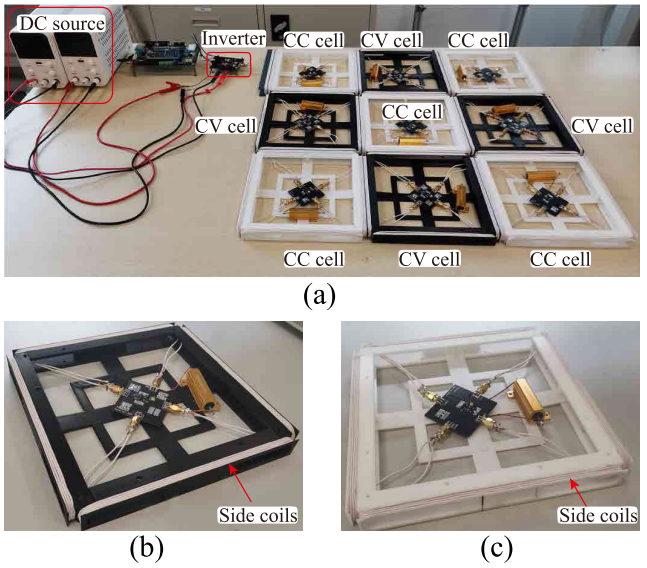

FIGURE 7. Prototype of a nine-cells 2-D IPT system. (a) system configuration. (b) A CV cell. (c) A CC cell.

IV. EXPERIMENTAL VALIDATION

In order to verify the proposed massive neighboring 2-D IPT system, a prototype with nine cells is implemented as shown in Fig. 7. The Litz wire with a diameter of 0.04 mm and 500 strands are used to make the coils to eliminate the skin effect. The multilayer ceramic capacitors from YAGEO Inc. are adopted to compensate for the circuit. The coil structures are identical to the simulation model in Section II-D, whose material is PLA (Polylactic Acid). The operating frequency is 1 MHz. Four GaNs transistors GS61008P (100V, 90A) form an H-bridge inverter to generate an ac power source at the targeted frequency. In each cell, the ac current and voltage

TABLE 2. Parameters of the experimental system.

Parameter	Value	Parameter	Value
V_{DC}	20 V	f_s	1 MHz
L	3.33 μH	C	7.6 nF
k	0.36	M	1.26 μH
r	173 mΩ	Q	120

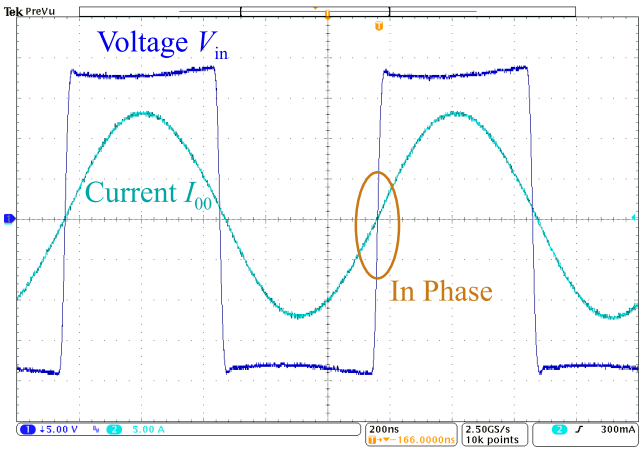

FIGURE 8. Input voltage V_{in} and current I_{00}.

are rectified to dc by a full bridge rectifier, which consists of four diodes (DFLS240L, 40V, 2A).

All the passive components like capacitors and inductors are measured by an impedance analyzer (WK6565-120, Wayne Kerr Electronics) under the operating frequency. Given some differences in the coil inductance, the compensation capacitors' values are finely tuned according to the specific inductance to satisfy the resonance condition. At the initial state, the dc load resistance in CC and CV cells are set to 5 Ω and 15 Ω, respectively. The detailed system parameters are listed in Table 2.

The waveform of input voltage V_{in} and current I_{00} is shown in Fig. 8. It can be observed that V_{in} and I_{00} are almost in phase, which means the power factor is near one. Besides, the waveform indicates that the zero-voltage switching (ZVS) condition is satisfied for the inverter, provided that an appropriate inductor is in series after the inverter. The experimental load current waveform of different CC cells and the voltage waveform of different CV cells is illustrated in Fig. 9(a) and (b), respectively. The currents and voltages have identical amplitudes and phases, respectively, as theoretically indicated in (9) and (10). The in-phase voltages in the CV cell and in-phase currents in the CC cell also suggest that each cell achieves ZPA condition.

The normalized output voltage/current distribution in 2-D plane is shown in Fig. 10(a). It shows that the cells farther away from the voltage source encounter more significant deviation than those near it. The loss breakdown of the proposed confronting-coil-based 2-D IPT system is shown in Fig. 11. The input power, the sum of powers in nine cells, and loss powers are 155, 116.3, and 38.7 W, respectively.

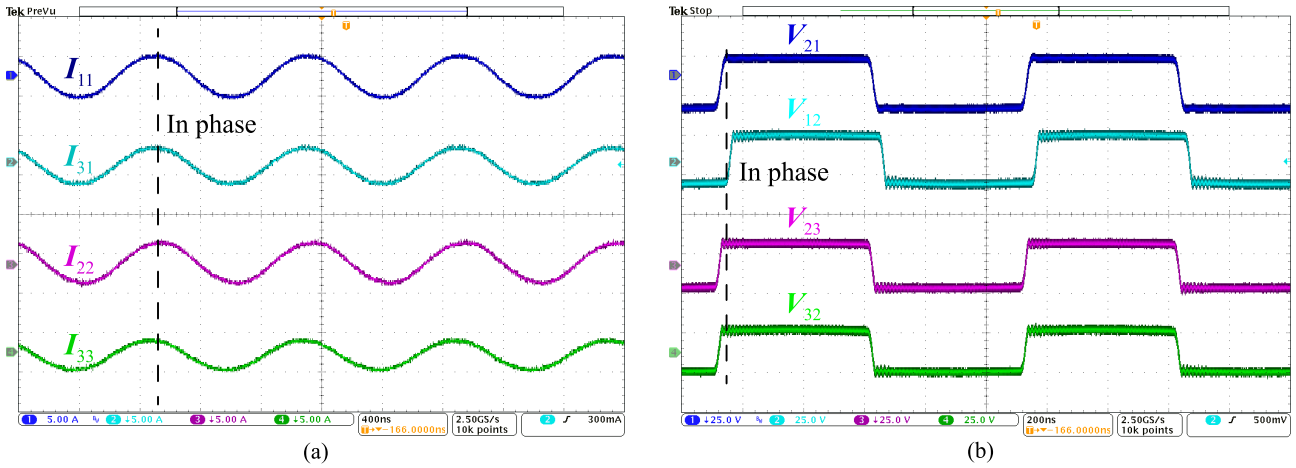

FIGURE 9. Experimental waveform. (a) The current waveform of four CC cells. (b) The voltage waveform of four CV cells.

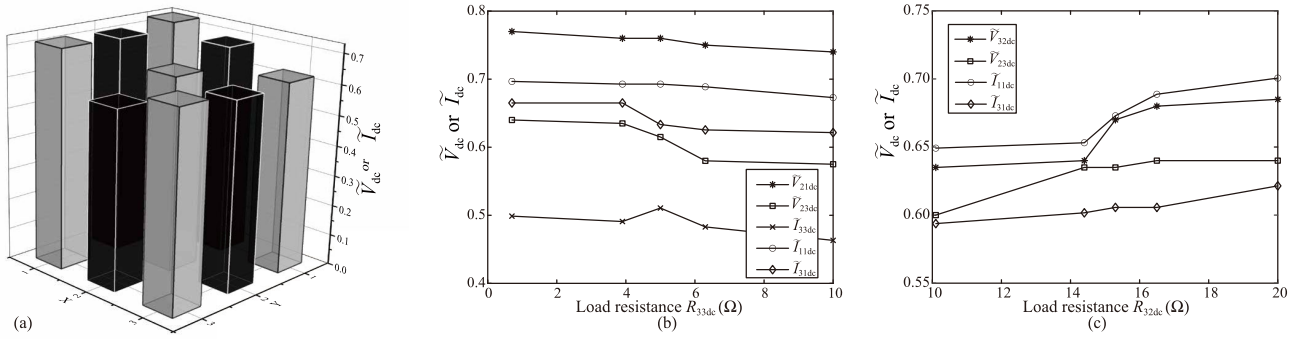

FIGURE 10. (a) Normalized output voltage/current of nine cells at initial state. (b) Normalized output voltage/current deviation when R_{33dc} varies. (c) Normalized output voltage/current deviation when R_{32dc} varies.

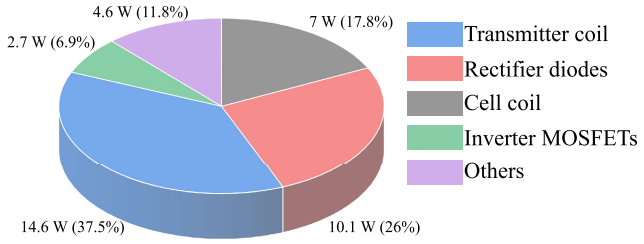

FIGURE 11. Experimental loss breakdown.

The overall conversion efficiency, considering the power losses of the inverter, resonant tank, and rectifier, achieves 75%.

One of the nine loads varies to examine the load variation rejection to further investigate the CC and CV properties. When the dc load R_{33dc} in the #33 CC cell varies from 1 Ω to 10 Ω and other loads remain unchanged, the corresponding normalized output dc voltage V_{mndc} and current I_{mndc} in the representative cells are illustrated in Fig. 10(b). Both the current and voltage only fluctuate in minimal ranges. The maximum current fluctuation is 0.12 A (4.8%) in the #33 cell, and the maximum voltage fluctuation is 1.3 V (6.5%) in the #23 cell.

To verify the CV property, while other load resistances are fixed at the initial state, the dc load in #32 cell varies from 10 Ω to 20 Ω. The normalized output voltage and the representative cells' normalized output current are shown in Fig. 10(c). The maximum current and voltage fluctuation are 0.13 A (5.1%) and 1 V (5%) in cells #11 and #32, respectively.

The results of the two cases suggest that the proposed 2-D IPT system can maintain relatively stable output despite load variations. In other words, the system strongly rejects the load variations. It achieves relatively stable CC and CV properties.

V. CONCLUSION

This paper proposed a two-dimensional (2-D) inductive power transfer (IPT) system for powering the massive neighboring IoT to meet the multiple-device power supply requirements. The inductor-capacitor (LC) resonators not only serve as relays but also power the load in each cell. The constant current (CC) and constant voltage (CV) properties were realized alternately in different cells in the proposed systems. The CC and CV properties enable a strong load-variation rejection

in all cells. Zero phase angle (ZPA) property was achieved so that any cells added or removed from the system will not affect the resonant state of the system. A 116 W nine-cells 2-D IPT prototype is manufactured to validate the proposed design. The overall conversion efficiency of the whole system is up to 75%

REFERENCES

[1] Y. Jiang, L. Wang, Y. Wang, J. Liu, X. Li, and G. Ning, "Analysis, design, and implementation of accurate ZVS angle control for EV battery charging in wireless high-power transfer," *IEEE Trans. Ind. Electron.*, vol. 66, no. 5, pp. 4075–4085, May 2019.

[2] J. H. Kim, B.-S. Lee, J.-H. Lee, S.-H. Lee, C.-B. Park, S.-M. Jung, S.-G. Lee, K.-P. Yi, and J. Baek, "Development of 1-MW inductive power transfer system for a high-speed train," *IEEE Trans. Ind. Electron.*, vol. 62, no. 10, pp. 6242–6250, Oct. 2015.

[3] J. Zhou, B. Zhang, W. Xiao, D. Qiu, and Y. Chen, "Nonlinear parity-time-symmetric model for constant efficiency wireless power transfer: Application to a drone-in-flight wireless charging platform," *IEEE Trans. Ind. Electron.*, vol. 66, no. 5, pp. 4097–4107, May 2019.

[4] H. H. Wu, G. A. Covic, J. T. Boys, and D. J. Robertson, "A series-tuned inductive-power-transfer pickup with a controllable AC-voltage output," *IEEE Trans. Power Electron.*, vol. 26, no. 1, pp. 98–109, Jan. 2011.

[5] Y. Zhang, T. Lu, Z. Zhao, K. Chen, F. He, and L. Yuan, "Wireless power transfer to multiple loads over various distances using relay resonators," *IEEE Microw. Wireless Compon. Lett.*, vol. 25, no. 5, pp. 337–339, May 2015.

[6] L. Sun, H. Tang, and S. Zhong, "Load-independent output voltage analysis of multiple-receiver wireless power transfer system," *IEEE Antennas Wireless Propag. Lett.*, vol. 15, pp. 1238–1241, 2016.

[7] M. Liu, M. Fu, Y. Wang, and C. Ma, "Battery cell equalization via megahertz multiple-receiver wireless power transfer," *IEEE Trans. Power Electron.*, vol. 33, no. 5, pp. 4135–4144, May 2018.

[8] C. Cheng, Z. Zhou, W. Li, C. Zhu, Z. Deng, and C. C. Mi, "A multi-load wireless power transfer system with series-parallel-series compensation," *IEEE Trans. Power Electron.*, vol. 34, no. 8, pp. 7126–7130, Aug. 2019.

[9] C. Cheng, F. Lu, Z. Zhou, W. Li, C. Zhu, H. Zhang, Z. Deng, X. Chen, and C. C. Mi, "Load-independent wireless power transfer system for multiple loads over a long distance," *IEEE Trans. Power Electron.*, vol. 34, no. 9, pp. 9279–9288, Sep. 2019.

[10] C. Cheng, F. Lu, Z. Zhou, W. Li, C. Zhu, Z. Deng, X. Chen, and C. Mi, "A multiload inductive power transfer repeater system with constant load current characteristics," *IEEE J. Emerg. Sel. Topics Power Electron.*, vol. 8, no. 4, pp. 3533–3541, Dec. 2020.

[11] C. Cheng, W. Li, Z. Zhou, Z. Deng, and C. Mi, "A load-independent wireless power transfer system with multiple constant voltage outputs," *IEEE Trans. Power Electron.*, vol. 35, no. 4, pp. 3328–3331, Apr. 2020.

[12] C. Cheng, Z. Zhou, W. Li, J. Lu, Z. Deng, and C. C. Mi, "Long-distance wireless power transfer system powering multiple loads with constant voltage outputs using S-SP compensation," *IET Power Electron.*, vol. 13, no. 9, pp. 1729–1734, Jul. 2020.

[13] C. Cheng, F. Lu, Z. Zhou, W. Li, Z. Deng, F. Li, and C. Mi, "A load-independent LCC-compensated wireless power transfer system for multiple loads with a compact coupler design," *IEEE Trans. Ind. Electron.*, vol. 67, no. 6, pp. 4507–4515, Jun. 2020.

[14] C. Cheng, Z. Zhou, W. Li, Z. Deng, and C. C. Mi, "A power relay system with multiple loads using asymmetrical coil design," *IEEE Trans. Ind. Electron.*, vol. 68, no. 2, pp. 1188–1196, 2021.

[15] C. Cheng, C. Wang, Z. Zhou, W. Li, Z. Deng, and C. C. Mi, "Repeater coil-based wireless power transfer system powering multiple gate drivers of series-connected IGBTs," *IET Power Electron.*, vol. 13, no. 9, pp. 1722–1728, Jul. 2020.

[16] Y. Gu, J. Wang, Z. Liang, Y. Wu, C. Cecati, and Z. Zhang, "Single-transmitter multiple-pickup wireless power transfer: Advantages, challenges, and corresponding technical solutions," *IEEE Ind. Electron. Mag.*, vol. 14, no. 4, pp. 123–135, Dec. 2020.

[17] Y. Wang, Z. Dongye, H. Zhang, C. Zhu, and F. Lu, "A domino-type load-independent inductive power transfer system with hybrid constant-current and constant-voltage outputs," *IEEE Trans. Power Electron.*, vol. 36, no. 8, pp. 8824–8834, Aug. 2021.

[18] F. S. Sandoval, S. M. T. Delgado, A. Moazenzadeh, and U. Wallrabe, "A 2-D magnetoinductive wave device for freer wireless power transfer," *IEEE Trans. Power Electron.*, vol. 34, no. 11, pp. 10433–10445, Nov. 2019.

[19] J. Feng, Q. Li, and F. C. Lee, "Load detection and power flow control algorithm for an omnidirectional wireless power transfer system," *IEEE Trans. Ind. Electron.*, vol. 69, no. 2, pp. 1422–1431, Feb. 2022.

[20] S. A. Mirbozorgi, H. Bahrami, M. Sawan, and B. Gosselin, "A smart multicoil inductively coupled array for wireless power transmission," *IEEE Trans. Ind. Electron.*, vol. 61, no. 11, pp. 6061–6070, Nov. 2014.

[21] X. Liu and G. Wang, "A novel wireless power transfer system with double intermediate resonant coils," *IEEE Trans. Ind. Informat.*, vol. 63, no. 4, pp. 2174–2180, Apr. 2016.

[22] J. Lee and K. Lee, "Effects of number of relays on achievable efficiency of magnetic resonant wireless power transfer," *IEEE Trans. Power Electron.*, vol. 35, no. 7, pp. 6697–6700, Jul. 2020.

[23] A. Wickramasinghe, R. L. S. Torres, and D. C. Ranasinghe, "Recognition of falls using dense sensing in an ambient assisted living environment," *Pervas. Mobile Comput.*, vol. 34, pp. 14–24, Jan. 2017.

[24] M. Daher, A. Diab, M. El Badaoui El Najjar, M. A. Khalil, and F. Charpillet, "Elder tracking and fall detection system using smart tiles," *IEEE Sensors J.*, vol. 17, no. 2, pp. 469–479, Jan. 2017.

[25] J. Cheng, M. Sundholm, B. Zhou, M. Hirsch, and P. Lukowicz, "Smart-surface: Large scale textile pressure sensors arrays for activity recognition," *Pervasive Mobile Comput.*, vol. 30, pp. 97–112, Aug. 2016.

[26] R. Serra, D. Knittel, P. Di Croce, and R. Peres, "Activity recognition with smart polymer floor sensor: Application to human footstep recognition," *IEEE Sensors J.*, vol. 16, no. 14, pp. 5757–5775, Jul. 2016.

[27] K. Mori, H. Lim, S. Iguchi, K. Ishida, M. Takamiya, and T. Sakurai, "Positioning-free resonant wireless power transmission sheet with staggered repeater coil array (SRCA)," *IEEE Antennas Wireless Propag. Lett.*, vol. 11, pp. 1710–1713, 2012.

[28] A. Hashizume, Y. Narusue, Y. Kawahara, and T. Asami, "Receiver localization for a wireless power transfer system with a 2D relay resonator array," in *Proc. IEEE Int. Conf. Comput. Electromagn. (ICCEM)*, Mar. 2017, pp. 127–129.

[29] K. Sumiya, T. Sasatani, Y. Nishizawa, K. Tsushio, Y. Narusue, and Y. Kawahara, "Alvus: A reconfigurable 2-D wireless charging system," *Proc. ACM Interact., Mobile, Wearable Ubiquitous Technol.*, vol. 3, no. 2, pp. 1–29, Jun. 2019.

[30] M. Morita, T. Sasatani, R. Takahashi, and Y. Kawahara, "Topology construction protocol for wireless power transfer system with a 2-D relay resonator array," in *Proc. IEEE Int. Conf. Consum. Electron. (ICCE)*, Jan. 2020, pp. 1–5.

[31] B. H. Waters, B. J. Mahoney, V. Ranganathan, and J. R. Smith, "Power delivery and leakage field control using an adaptive phased array wireless power system," *IEEE Trans. Power Electron.*, vol. 30, no. 11, pp. 6298–6309, Nov. 2015.

[32] International Commission on Non-Ionizing Radiation Protection, "Guidelines for limiting exposure to electromagnetic fields (100 kHz to 300 GHz)," *Health Phys.*, vol. 118, no. 5, pp. 483–524, May 2020.

[33] T. Sasatani, Y. Narusue, and Y. Kawahara, "Genetic algorithm-based receiving resonator array design for wireless power transfer," *IEEE Access*, vol. 8, pp. 222385–222396, 2020.

YIMING GAO received the B.S. and B.L. degrees from the Qingdao University of Technology, Qingdao, China, in 2018. He is currently pursuing the Ph.D. degree with ShanghaiTech University, China. His research interests include wireless power transfer, simulation, and design algorithms for power & energy circuits and systems.

MINFAN FU (Senior Member, IEEE) received the B.S., M.S., and Ph.D. degrees in electrical and computer engineering from the University of Michigan—Shanghai Jiao Tong University Joint Institute, Shanghai Jiao Tong University, Shanghai, China, in 2010, 2013, and 2016, respectively. From 2016 to 2018, he was a Postdoctoral Researcher with the Center for Power Electronics Systems, Virginia Polytechnic Institute, and State University, Blacksburg, VA, USA. He is currently an Assistant Professor at the School of Information Science and Technology, ShanghaiTech University, Shanghai. He holds one U.S. patent, and three Chinese patents, and has authored or coauthored more than 50 papers in prestigious IEEE journals and conferences. His research interests include megahertz wireless power transfer, high-frequency power conversion, high-frequency magnetic design, and the application of wide-bandgap devices. He is currently an Associate Editor for the IEEE IES Industrial Electronics Technology News and serves as the Section Chair of several conferences, such as IECON, IPEMC, and VEH. His Conference Paper for IECON 2019 won the IES-SYPA Competition. He is the Tutorial Speaker for IPEMC 2020 and ISIE 2020.

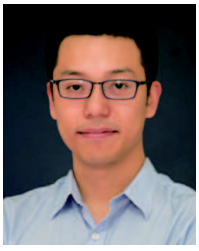

HAOYU WANG (Senior Member, IEEE) received the bachelor's degree (Hons.) in electrical engineering from Zhejiang University, Hangzhou, China, in 2009, and the Ph.D. degree in electrical engineering from the University of Maryland at College Park, College Park, MD, USA, in 2014. In 2014, he joined the School of Information Science and Technology, ShanghaiTech University, Shanghai, China, where he is currently a tenured Associate Professor. His research interests include power electronics, plug-in electric and hybrid electric vehicles, the applications of wide-bandgap semiconductors, renewable energy harvesting, and power management integrated circuits. He is an Associate Editor for IEEE TRANSACTIONS ON INDUSTRIAL ELECTRONICS, IEEE TRANSACTIONS ON TRANSPORTATION ELECTRIFICATION, and *CPSS Transactions on Power Electronics and Applications*.

JUNRUI LIANG (Senior Member, IEEE) received the B.E. and M.E. degrees in instrumentation engineering from Shanghai Jiao Tong University, Shanghai, China, in 2004 and 2007, respectively, and the Ph.D. degree in mechanical and automation engineering from The Chinese University Hong Kong, Hong Kong, China, in 2010. He is currently an Associate Professor at the School of Information Science and Technology, ShanghaiTech University, Shanghai. His research interests include energy conversion and power conditioning circuits, kinetic energy harvesting and vibration suppression, the IoT devices, and mechatronics.

He is an Associate Editor of *IET Circuits, Devices and Systems* and the General Chair of the 2nd International Conference on Vibration and Energy Harvesting Applications (VEH) 2019. He was a recipient of three best paper awards, in 2009 and 2010 IEEE International Conference on Information and Automation, and the 2021 International Conference on Vibration Energy Harvesting and Applications, respectively.